A coupled elastoplastic-damage constitutive model with Lode angle dependent failure criterion

Borja Erice , Francisco Gálvez

A B S T R A C T

A coupled elastoplastic-damage constitutive model with Lode angle dependent failure criterion for high strain and ballistic applications is presented. A Lode angle dependent function is added to the equivalent plastic strain to failure definition of the Johnson–Cook failure criterion. The weakening in the elastic law and in the Johnson–Cook-like constitutive relation implicitly introduces the Lode angle dependency in the elastoplastic behaviour. The material model is calibrated for precipitation hardened Inconel 718 nickel-base superalloy. The combination of a Lode angle dependent failure criterion with weakened constitutive equations is proven to predict fracture patterns of the mechanical tests performed and provide reliable results. Additionally, the mesh size dependency on the prediction of the fracture patterns was studied, showing that was crucial to predict such patterns.

Keywords:
Weakening
Nickel-base superalloy
Finite element
High strain rate
Constitutive equations

1. Introduction

The material models that are typically used for the ductile metals may be classified according to their formulation as uncoupled and coupled. In the former the failure criterion does not affect to the constitutive relationships, whereas in the latter the accumulated damage weakens somehow the elastic moduli, the constitutive relationships or both. Several uncoupled material models with third deviatoric invariant dependent yield function and failure criterion can be found in the literature such as the published by Wilkins et al. (1980), Bai and Wierzbicki (2008) or Bai and Wierzbicki (2010). Nevertheless, such models are not the only ones that account for the third invariant dependency. Other uncoupled models with independent failure criteria also can be found. In a recent investigation, Kane et al. (2011) used a Johnson–Cook-like constitutive relationship combined with two uncoupled failure criteria: Cockcroft–Latham (Cockcroft and Latham, 1968) criterion and a Continuum Damage Mechanics (CDM) based criterion (Lemaitre, 1996). They show the effect that the Lode parameter has in the fracture strain. Conversely, the coupled models prefer to employ classical metal yield functions such and von Mises yield function and insert the third invariant in the plasticity through elastoplastic-damage coupled constitutive relationships. That is the case of the models proposed Wierzbicki and Xue (Xue, 2007; Xue and Wierzbicki, 2008) or Nahshon and Hutchinson (2008). The conclusion achieved by all the authors using all those material models is almost equivalent. The third deviatoric invariant should be introduced in the model if complex fracture patterns are to be captured.

In the recently postulated JCX model by Chocron et al. (2011), the introduction of the third deviatoric invariant in the uncoupled Johnson–Cook model was investigated. In accordance with the previously stated, one of the conclusions that such research arose was that it was not possible to obtain complex fracture patterns unless the third invariant was somehow included in the plasticity model. In the JCX material model the third invariant was added by using a Lode angle dependent function. This formulation implied a non-convex yield surface. Although it was demonstrated that it was a perfectly valid formulation, non-convex yield surfaces are unorthodox in metal plasticity. With the same background, a new formulation using a von Mises yield surface and a coupled elastoplastic-damage constitutive model is now proposed.

Since the model is intended for high strain rate phenomena and ballistic applications, the Johnson–Cook model (Johnson and Cook, 1985, 1983) is taken as a basis. The objective is to use a Lode angle dependent function only in the definition of the equivalent plastic strain to failure. The coupled elastoplastic-damage constitutive model, similar to the damage coupled Johnson–Cook model presented by Børvik et al. (2001), carries out the rest. The influence of third deviatoric invariant is then implicitly included with the help of the coupled relationship. The concept of including the third deviatoric invariant in such a way to obtain complex fracture patterns like slanted cracks, was ascertained by Xue and Wierzbicki (2009).

An extensive experimental campaign was carried out in order to calibrate the postulated model for the precipitation hardened Inconel 718 nickel-base superalloy. The mechanical tests were performed by employing different geometries and testing techniques. Therefore, they were divided in the three following groups:

- Quasi-static tensile tests of axisymmetric smooth and notched specimens at room temperature.
- Quasi-static tensile tests of plane specimens.
- Dynamic tests of smooth axisymmetric specimens at various temperatures.

Numerical simulations of all the tests using the explicit version of LS-DYNA non-linear finite element code were carried out in order to check the validity of the model. The capability of the proposed material model in terms of reproducing fracture patterns was also studied. The effect of the mesh size on such patterns was found as crucial.

2. The model

2.1. Stress invariant representation

Any yield surface can be described by using the $\boldsymbol{\sigma}$ stress tensor invariants I_1, I_2 and I_3 (Souza et al., 2008). This representation is extremely useful, given that in most of the cases it is associated to a geometric interpretation in the principal stress space. A scalar yield function $\phi(I_1, I_2, I_3)$ represents a surface in the principal stress space $(\sigma_1, \sigma_2, \sigma_3)$. Nevertheless, a combination of another three invariants (σ_H, J_2, θ) is more common. Thus, the yield function can also be a function of them as:

$$\phi = \phi(I_1, I_2, I_3) = \phi(\sigma_H, J_2, \theta) \tag{1}$$

where $\sigma_H = 1/3 I_1 = 1/3\,\mathrm{tr}(\boldsymbol{\sigma})$ is the hydrostatic stress, J_2 is the second deviatoric stress invariant and θ is the Lode angle. The first invariant is related with the stress tensor, whereas the other two are related with the deviatoric stress tensor.

In metals, this dependency is usually neglected (Hill, 1950). Therefore, for metal plasticity the yield function can be written as $\phi(J_2, \theta)$. As an example, two of the most extensively used yield functions are depicted in Fig. 1, von Mises and Tresca yield criterion. The former is only J_2 dependent, whereas the latter is J_2, θ dependent.

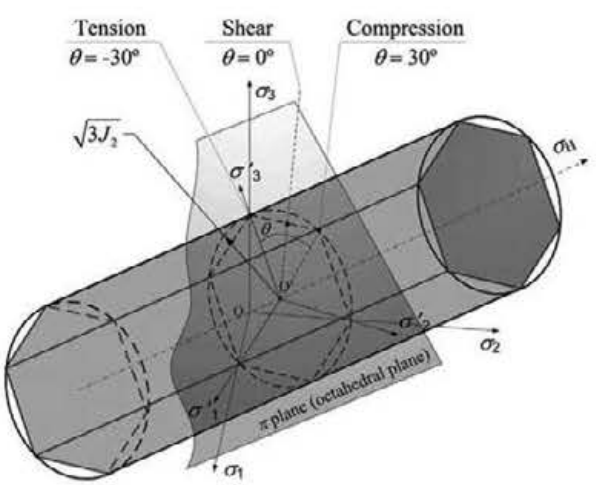

Fig. 1. von Mises and Tresca yield criteria. Geometric interpretation of the three invariants (σ_H, J_2, θ) in the principal stress space.

The second and third deviatoric stress invariants J_2 and J_3, respectively are:

$$J_2 = -I_2(\boldsymbol{\sigma}') = \frac{1}{2}\mathrm{tr}(\boldsymbol{\sigma}'^2) = \frac{1}{2}\boldsymbol{\sigma}' : \boldsymbol{\sigma}' \tag{2}$$

$$J_3 = I_3(\boldsymbol{\sigma}') = \det(\boldsymbol{\sigma}') = \frac{1}{3}\mathrm{tr}(\boldsymbol{\sigma}')^3 \tag{3}$$

Typically, the third invariant is not used *per se* in the formulation of the yield function. Another invariant is used in exchange, the Lode angle. The main reason is that this last invariant has a clear geometric interpretation in the principal stress space. The Lode angle θ is:

$$\theta = -\frac{1}{3}\sin^{-1}\left(\frac{3\sqrt{3}J_3}{2J_2^{3/2}}\right) = -\frac{1}{3}\sin^{-1}\left(\frac{27J_3}{2\overline{\sigma}^3}\right) \tag{4}$$

The Lode angle takes values from $-\pi/6 \leqslant \theta \leqslant \pi/6$ $(-30^\circ \leqslant \theta \leqslant 30^\circ)$, with the angle being between $\boldsymbol{\sigma}'$ and nearest pure shear line (see Fig. 1). According to the definition, $\theta = -30^\circ$ represents an axisymmetric tensile stress state, while $\theta = 30^\circ$ represents an axisymmetric compression stress state. Between them, $\theta = 0^\circ$ is for a pure shear stress state.

Since the Lode angle represents the different stress states can be also used to define the strain to failure. Most ductile fracture criteria are based on nucleation, growth and coalescence of voids. The void growth inside the material is considered to be stress triaxiality-driven. Hence, the strain to failure can also be expressed as a function of the stress triaxility $\sigma^* = \sigma_H/\overline{\sigma}$ and the Lode angle.

2.2. Constitutive model

The model was designated as Johnson–Cook–Xue-damage (JCXd) to distinguish it from the uncoupled version JCX postulated by Chocron et al. (2011). The details of the numerical implementation can be found in Erice (2012).

Assuming the additive decomposition of the strain tensor as:

$$\boldsymbol{\varepsilon} = \boldsymbol{\varepsilon}^e + \boldsymbol{\varepsilon}^p \tag{5}$$

the coupled elastic-damaged law reads:

$$\boldsymbol{\sigma} = w(D)\mathbf{C} : \boldsymbol{\varepsilon}^e = w(D)\mathbf{C} : (\boldsymbol{\varepsilon} - \boldsymbol{\varepsilon}^p) \tag{6}$$

where $w(D)$ is the weakening function defined as:

$$w(D) = 1 - D^\beta \tag{7}$$

where D is the damage parameter and β is a material constant. $\mathbf{C}$ is the fourth-order isotropic tensor of elastic moduli given by:

$$\mathbf{C} = \left(K - \frac{2G}{3}\right)\boldsymbol{I} \otimes \boldsymbol{I} + 2G\boldsymbol{I} = \frac{vE}{(1+v)(1-2v)}\boldsymbol{I} \otimes \boldsymbol{I} + \frac{E}{(1+v)}\boldsymbol{I} \tag{8}$$

where E is the elastic modulus, v is the Poisson's ratio, G is the shear modulus and K is the bulk modulus.

A classical metal plasticity yield function was adopted to model the plastic flow, i.e. the von Mises yield function. For the JCXd material model the yield function is:

$$\phi(\boldsymbol{\sigma}, Y^{JCXd}) = \phi(J_2, \bar{\varepsilon}_p, \dot{\bar{\varepsilon}}_p, T, D) = \overline{\sigma}(\boldsymbol{\sigma}) - Y^{JCXd}(\bar{\varepsilon}_p, \dot{\bar{\varepsilon}}_p, T, D) \tag{9}$$

where is $\overline{\sigma} = \sqrt{3J_2}$ the equivalent stress and Y^{JCXd} is the JCXd flow stress defined as:

$$Y^{JCXd}(\bar{\varepsilon}_p, \dot{\bar{\varepsilon}}_p, T, D) = w(D)Y_M(\bar{\varepsilon}_p, \dot{\bar{\varepsilon}}_p, T) \tag{10}$$

where Y_M represents the matrix material hardening. The hardening of the matrix material was modelled by using a Johnson–Cook-like relationship (Johnson and Cook, 1983) as follows:

$$Y_M = Y^{JC}(\bar{\varepsilon}_p, \dot{\bar{\varepsilon}}_p, T) = [A + B\bar{\varepsilon}_p^n][1 + C\ln\dot{\bar{\varepsilon}}_p^*][1 - T^{*m}] \tag{11}$$

where A, B, n, C and m are material constants, $\dot{\bar{\varepsilon}}_p^* = \dot{\bar{\varepsilon}}_p/\dot{\varepsilon}_0$ is the dimensionless plastic strain rate, $\dot{\varepsilon}_0$ is the reference strain rate, $T^* = (T - T_r)/(T_r - T_m)$ is the homologous temperature, T is the current temperature and T_r is the room or reference temperature. T_m is the melting temperature, which is defined as the temperature for which the material holds no strength, i.e. $Y_M = 0$. The only difference with the original Johnson–Cook relationship is the introduction of the initial temperature T_0, which allows to have the elements initially at the user-designated temperature maintaining T_r constant.

The flow rule chosen was associative. Therefore, the plastic strain rate tensor is defined as follows:

$$\dot{\boldsymbol{\varepsilon}}^p = \dot{\lambda}\frac{\partial\phi(\boldsymbol{\sigma}, Y^{JCXd})}{\partial\boldsymbol{\sigma}} \tag{12}$$

2.3. Failure criterion and evolution of the internal variables

The set of internal variables chosen for the present model is:

$$\boldsymbol{\alpha} = \{\bar{\varepsilon}_p, D\} \tag{13}$$

where $\bar{\varepsilon}_p$ is the equivalent plastic strain and D is the damage parameter. The generalised hardening modulus (Souza et al., 2008) is then composed by:

$$\boldsymbol{H} = \{H_1, H_2\} \tag{14}$$

The evolution law for the equivalent plastic strain is:

$$\begin{aligned} \dot{\bar{\varepsilon}}_p &= \dot{\lambda} \\ H_1 &= 1 \end{aligned} \tag{15}$$

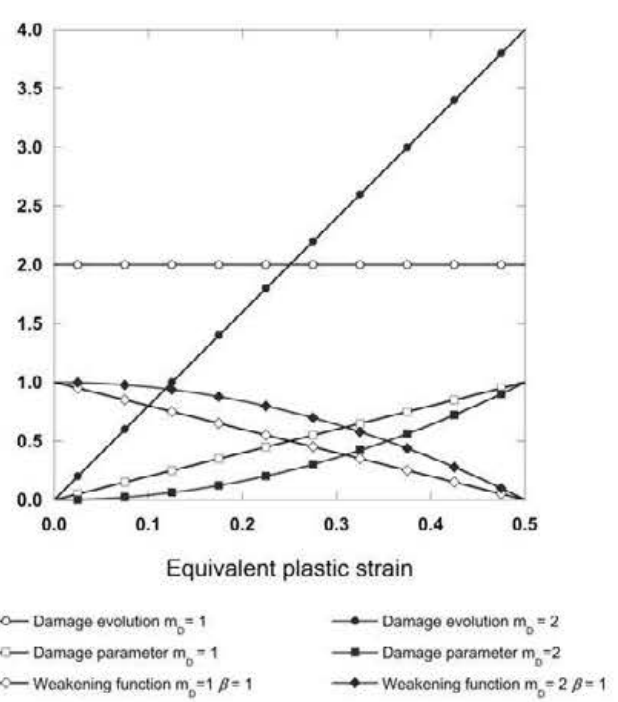

Fig. 2. Damage evolution, damage parameter and weakening function as a function of equivalent plastic strain for a constant equivalent plastic strain to failure of 0.5.

The evolution law for the damage parameter was defined by Xue (2007) and may be described as follows:

$$\begin{aligned} \dot{D} &= \dot{\lambda}H_2 = m_D(\bar{\varepsilon}_p)^{m_D-1}\left(\frac{1}{\bar{\varepsilon}_p^{fJCXd}(\sigma^*, \dot{\bar{\varepsilon}}_p, T, \theta)}\right)^{m_D}\dot{\bar{\varepsilon}}_p \\ H_2 &= m_D(\bar{\varepsilon}_p)^{m_D-1}\left(\frac{1}{\bar{\varepsilon}_p^{fJCXd}(\sigma^*, \dot{\bar{\varepsilon}}_p, T, \theta)}\right)^{m_D} \end{aligned} \tag{16}$$

where m_D is a material constant and $\bar{\varepsilon}_p^{fJCXd}$ is the equivalent plastic strain to failure. The versatility of this expression lies in the constant m_D. Such a constant allows shaping the damage accumulation as a function of the equivalent plastic strain as can be seen in Fig. 2. For example, for $m_D = 1$ the damage accumulation is linear, while for $m_D = 2$ the damage accumulation is quadratic. Note that for $m_D = 1$ the Johnson–Cook damage evolution law is recovered.

The expression for the equivalent plastic strain to failure $\bar{\varepsilon}_p^{fJCXd}$ is:

$$\bar{\varepsilon}_p^{fJCXd} = \bar{\varepsilon}_p^{fJCX} = \bar{\varepsilon}_p^{fJC}\mu_\theta(\theta) \tag{17}$$

where μ_θ is the second kind of the Lode angle dependent function (Xue, 2007), $\bar{\varepsilon}_p^{fJCX}$ is the equivalent plastic strain defined for the JCX model and $\bar{\varepsilon}_p^{fJC}$ is the equivalent plastic strain of the Johnson–Cook model given by:

$$\bar{\varepsilon}_p^{fJC}(\sigma^*, \dot{\bar{\varepsilon}}_p, T) = [D_1 + D_2\exp(D_3\sigma^*)][1 + D_4\ln\dot{\bar{\varepsilon}}_p^*][1 + D_5T^*] \tag{18}$$

where D_1, D_2, D_3, D_4 and D_5 are material constants, $\sigma^* = \sigma_H/\bar{\sigma}$ is the stress triaxiality ratio. $\dot{\bar{\varepsilon}}_p^*$ and T^* are identical as those variables previously.

The second kind of Lode angle is one of the two different interpolating functions proposed by Xue (2007). In this case, the function interpolates the equivalent plastic strain to failure corresponding to the different stress states. It is defined as:

$$\mu_\theta = \gamma + (1 - \gamma)\left(\frac{6|\theta|}{\pi}\right)^k \tag{19}$$

where $\gamma = \bar{\varepsilon}_p^{fS}(\sigma^*)/\bar{\varepsilon}_p^{fTC}(\sigma^*)$, is the relative ratio between the equivalent plastic strain to failure corresponding to a generalised shear (upper-script S) and an axisymmetric tension (upper-script T) or compression (upper-script C) stress states. It should be noted that for the sake of simplicity k has been set to the unity.

The evolution law for the temperature is given by:

$$\dot{T} = \frac{\chi}{\rho C_p}\boldsymbol{\sigma} : \dot{\boldsymbol{\varepsilon}}^p \tag{20}$$

The expression of the plastic multiplier comes from the consistency condition ($\dot{\phi} = 0$). The consistency condition for the postulated yield function is:

$$\begin{aligned} \dot{\phi} &= \frac{\partial\phi}{\partial\boldsymbol{\sigma}} : \mathbf{C} : (\dot{\boldsymbol{\varepsilon}} - \dot{\lambda}\boldsymbol{N}) + \dot{\lambda}\frac{\partial\phi}{\partial\bar{\varepsilon}_p}H_1 + \dot{\lambda}\frac{\partial\phi}{\partial D}H_2 = \frac{\partial\phi}{\partial\boldsymbol{\sigma}} : \mathbf{C} : (\dot{\boldsymbol{\varepsilon}} - \dot{\lambda}\boldsymbol{N}) \\ &\quad + \dot{\lambda}\left(\frac{\partial\phi}{\partial Y^{JCXd}}\frac{\partial Y^{JCXd}}{\partial\bar{\varepsilon}_p}H_1 + \frac{\partial\phi}{\partial Y^{JCXd}}\frac{\partial Y^{JCXd}}{\partial w}\frac{\partial w}{\partial D}H_2\right) \\ &= \frac{\partial\phi}{\partial\boldsymbol{\sigma}} : \mathbf{C} : (\dot{\boldsymbol{\varepsilon}} - \dot{\lambda}\boldsymbol{N}) - \dot{\lambda}\left(w\frac{\partial Y_M}{\partial\bar{\varepsilon}_p}H_1 - Y_M\frac{\partial w}{\partial D}H_2\right) \\ &= \frac{\partial\phi}{\partial\boldsymbol{\sigma}} : \mathbf{C} : (\dot{\boldsymbol{\varepsilon}} - \dot{\lambda}\boldsymbol{N}) - \dot{\lambda}(wHH_1 - \beta D^{\beta-1}Y_MH_2) = 0 \end{aligned} \tag{21}$$

where H is the hardening modulus of the matrix material $H = \partial Y_M/\partial\bar{\varepsilon}_p$. Operating in the expression above the plastic multiplier can be obtained as:

$$\dot{\lambda} = \frac{\frac{\partial\phi}{\partial\boldsymbol{\sigma}} : \mathbf{C} : \dot{\boldsymbol{\varepsilon}}}{\frac{\partial\phi}{\partial\boldsymbol{\sigma}} : \mathbf{C} : \boldsymbol{N} + wHH_1 - \beta D^{\beta-1}Y_MH_2} \tag{22}$$

3. Material description

The material tested was a wrought polycrystalline nickel-base superalloy. The commercial designation for such a superalloy is Inconel 718. The chemical composition in weight percentage is summarised in Table 1. The alloy was precipitation hardened according to the heat treatment summarised in Table 2. The precipitation hardened Inconel 718 nickel-base superalloy is commonly employed to manufacture components that work with relatively high temperatures. Some examples of jet engine components are turbine casings or high pressure compressor rotor blades.

4. Experiments

The consequence of the introduction of a Lode angle dependent function in the model is that more points in the equivalent plastic strain to failure vs. triaxiality space are needed to calibrate the failure criterion. The tensile tests of axisymmetric smooth and notched specimens are enough to calibrate triaxiality dependent failure criteria as Johnson–Cook (Johnson and Cook, 1985) or Rice–Tracey (Rice and Tracey, 1969) criteria. The axisymmetric notched specimens provide different triaxialities depending on their notch radius (Bridgman, 1952). Nevertheless, all present the same Lode angle value, $\theta = -30°$ (Bai and Wierzbicki, 2008). Therefore, additional tests are required to calibrate Lode dependent failure criteria.

To complete those additional tests, two approaches are customarily adopted. The first one consists of using machines that allow performing tests with combined stress states (multi-axial, tension-shear, amongst others). As an example, the reader is referred to the combined tension-torsion experiments carried out by Barsoum and Faleskog (2007). The second approach, and relatively more simple, consists of designing a specimen geometry capable of developing the desired stress state in its gauge area. Shear and plane strain specimens are those most widely employed. Many tested shear specimens have been designed (Bai and Wierzbicki, 2008; Bao and Wierzbicki, 2004; Eriksson et al., 2006; Mae et al., 2007).

Three groups of tests were performed for the calibration of the JCXd material model for the precipitation hardened Inconel 718 nickel-base superalloy. The first group was composed of quasi-static tensile tests of axisymmetric smooth and notched specimens. The second group was constituted of quasi-static plane specimens: shear and plane strain. Finally, the third entailed dynamic tensile tests of smooth axisymmetric specimens.

4.1. Quasi-static tests of axisymmetric smooth and notched specimens

The geometry and dimensions of the axisymmetric smooth and notched specimens employed are depicted in Fig. 3(a) and (b), respectively. The tensile tests were conducted in a universal screw-driven testing machine at a strain rate of $1.0 \times 10^{-3}\,s^{-1}$. Three geometries of axisymmetric specimens were tested: smooth, notch radius $R = 2$ mm and notch radius $R = 0.8$ mm.

Initial triaxiality values were analytically calculated using Bridgman's analysis for axisymmetric notched specimens:

$$\sigma^* = \frac{1}{3} + \ln\left(1 + \frac{r}{2R}\right) \tag{23}$$

where r is the initial cross-section radius and R is the notch radius. For all the specimens the initial Lode angle value was $\theta = -30°$ (see Table 3).

The minimum cross-section diameter of the specimens was monitored during the tests. The measures were performed by employing two perpendicularly located laser-based micrometres mounted on a mobile frame. The mobility of the frame allowed measuring the minimum cross-section diameter at all times. Such diameter measurement was used to calculate true stress and strain values until failure as:

$$\sigma = \frac{F}{\pi d^2/4} \tag{24}$$

$$\varepsilon = 2\ln\left(\frac{d_0}{d}\right) \tag{25}$$

where d_0 and d are the initial and current values of the minimum cross-section diameter, respectively, F is the load red from the load cell. Assuming the additive decomposition of the strains, the true plastic strain ε_p was calculated as:

$$\varepsilon_p = \varepsilon - \varepsilon_e = \varepsilon - \sigma/E \tag{26}$$

where ε_e is the elastic strain and E is the elastic modulus. The true stress–strain and stress–plastic strain curves of the tensile tests performed with the smooth and notched axisymmetric specimens are depicted in Fig. 4(a) and (b), respectively.

4.2. Dynamic tests of axisymmetric smooth specimens at various temperatures

A Split Hopkinson Tension Bar (SHTB) was used to carry out dynamic tensile tests of axisymmetric smooth specimens. The geometry and dimensions of the specimens employed are shown in Fig. 3(c). The dimensions and set-up of the SHTB can be seen in Fig. 6. The tests were conducted at an approximate strain rate of $1.0 \times 10^{3}\,s^{-1}$.

A temperature chamber was installed in the SHTB (see Fig. 5) to perform the mechanical testing of the specimens at various temperatures. The temperature chamber was controlled by a thermocouple attached to the specimen. In order to maintain the properties of the bars as constant as possible with the temperature, two René 41 nickel-base super-alloy bars were used as input and output bars. The mass density and the elastic modulus of the René 41 bars were $\rho_b = 8240\,kg/m^3$ and $E_b = 218$ GPa, respectively.

Table 1
Certificated chemical composition in %wt. of Inconel 718 nickel-base superalloy.

Cr	Ni	Mo	Nb	Ti	Al	F	C	Cu
19.0	52.5	3.0	5.1	0.9	0.5	18.5	0.08max	0.15max

Table 2
Heat treatment chart for the precipitation hardening of the Inconel 718 nickel-base superalloy.

Process number	Initial temperature (°C)	Final temperature (°C)	Vacuum level (mbar)	Process mode	Velocity	Time (h)
1	25	720	$>10^{-4}$	Heating	10 C/min. or max. velocity	
2	720	720	$>10^{-4}$	Maintain		8
3	720	620	$>10^{-4}$	Cooling	~1 C/h	
4	620	620	$>10^{-4}$	Maintain		8
5	620	RT		Cooling	max. velocity air cool	

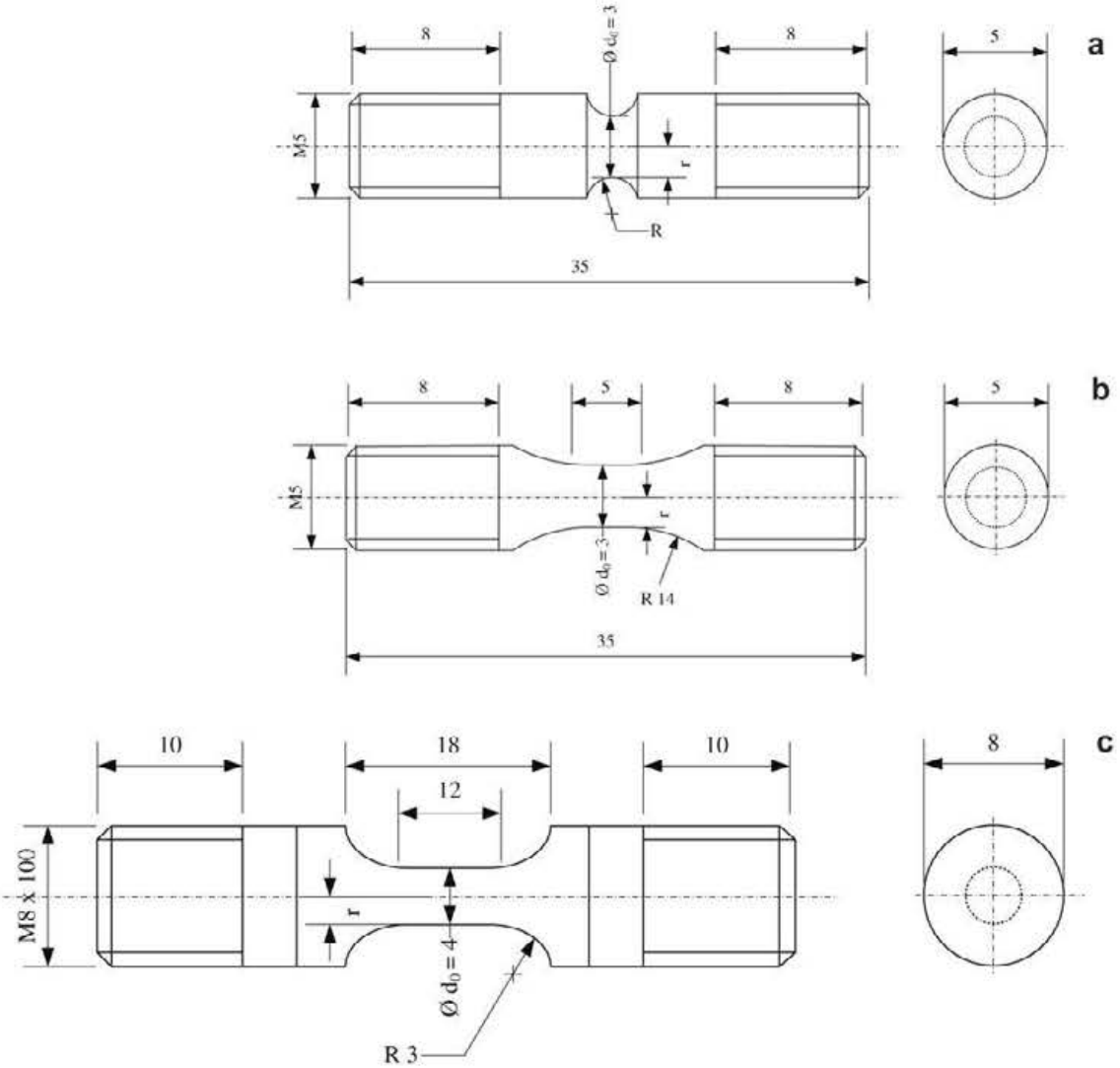

Fig. 3. Dimensions and geometry of the axisymmetric smooth (a) and notched (b) specimens used for the quasi-static tensile tests and axisymmetric smooth specimens (c) used for the dynamic tests at various temperatures.

Table 3
Triaxiality ratio, Lode angle and equivalent plastic strain to failure data from the experimental data and from numerical simulations.

Specimen	Analytical				Numerical simulations		
	σ^*	$\theta(^\circ)$	$\overline{\varepsilon}_p^f$	$T_f(^\circ C)$	σ^*	$\theta(^\circ)$	$\overline{\varepsilon}_p^f$
Quasi-static regime $\dot{\varepsilon} = 1.0 \times 10^{-3}\ s^{-1}$							
Smooth	1/3	−30	0.320	25	0.615	−30	0.342
Notched $R = 2$ mm	0.652	−30	0.138	25	1.337	−30	0.135
Notched $R = 0.8$ mm	0.995	−30	0.120	25	1.650	−30	0.137
Shear	0.000	0	1.100	25	−0.018	−0.018	1.157
Plain strain	0.577	0	0.425	25	0.871	−1.551	0.401
Dynamic regime $\dot{\varepsilon} = 1.0 \times 10^{3}\ s^{-1}$							
Smooth $T_0 = 25$ °C	1/3	−30	0.517	282	0.800	−30	0.504
Smooth $T_0 = 394$ °C	1/3	−30	0.600	282	0.850	−30	0.550
Smooth $T_0 = 589$ °C	1/3	−30	0.662	636	0.840	−30	0.616
Smooth $T_0 = 691$ °C	1/3	−30	0.693	810	0.841	−30	0.630
Smooth $T_0 = 781$ °C	1/3	−30	0.697	909	0.845	−30	0.660

The specimens were tested at room temperature, 394 °C, 589 °C, 691 °C and 781 °C. The input bar was 8050 mm in length and the output 3850 mm. The diameter of both bars was 19.30 mm. The striker bar was a 2000 mm long tubular bar. It was launched with compressed air in the opposite direction of the wave propagation. The striker bar impact caused a tensile elastic wave, the incident wave. With this SHTB configuration the incident wave pulse length was around 800 μs. The wave travelled along the input bar until it

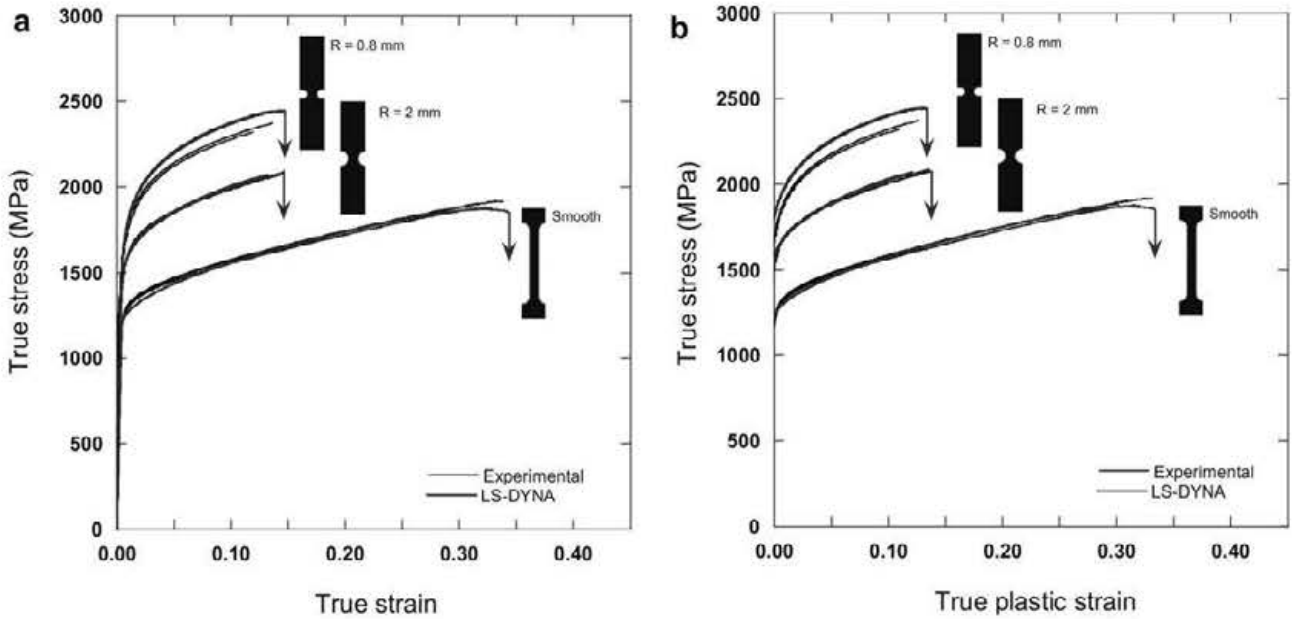

Fig. 4. (a) True stress–strain and (b) true stress–plastic strain curves of the smooth axisymmetric specimens and notched axisymmetric specimens with notch radius $R = 2$ mm and $R = 0.8$ mm tested at a strain rate of $1.0 \times 10^{-3}\,s^{-1}$ compared with the numerical simulations.

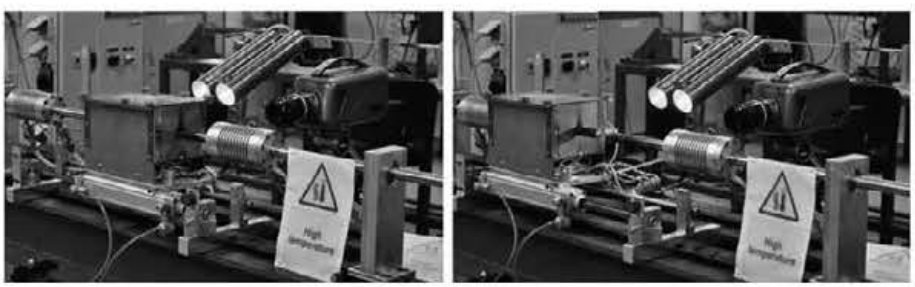

Fig. 5. Standard experimental set-up for the SHTB. The equipment includes high-powered lamps, Phantom v12 high-speed camera and a temperature chamber. Temperature chamber is shown in (a) closed position and (b) opened position.

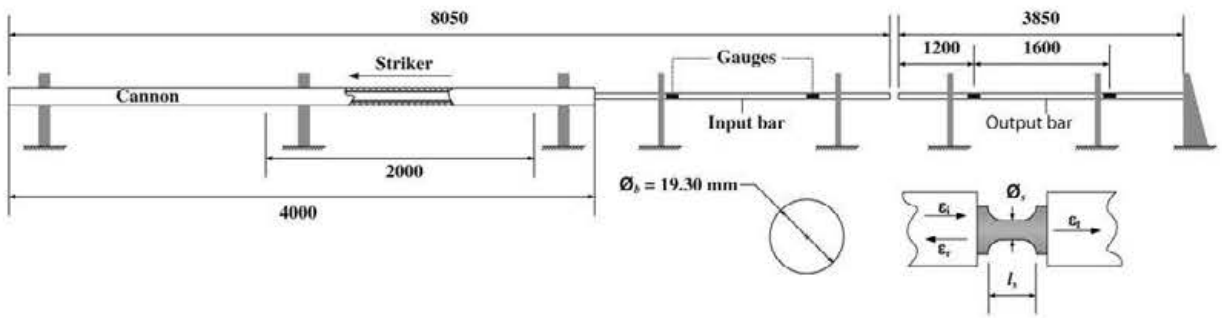

Fig. 6. Schematic view of the tensile SHTB used to carry out the dynamic tests. Detailed view of the specimen with input and output bars showing incident, reflected and transmitted.

reached the specimen. Material and geometry mismatch caused a reflected and transmitted wave. These three waves could be decomposed in strains which affect input and output bars. Incident (ε_i) and reflected (ε_r) strains affect the input bar and transmitted strain affects (ε_t) the output bar. The strain history was recorded with strain gauges attached to the input and output bars (see Fig. 6). The use of strains or stresses is equivalent, given that the bars are constantly in elastic regime. According to the elastic one-dimensional wave propagation theory and its application to the SHTB (Kolsky, 1963):

$$\varepsilon_i + \varepsilon_r = \varepsilon_t \tag{4.1}$$

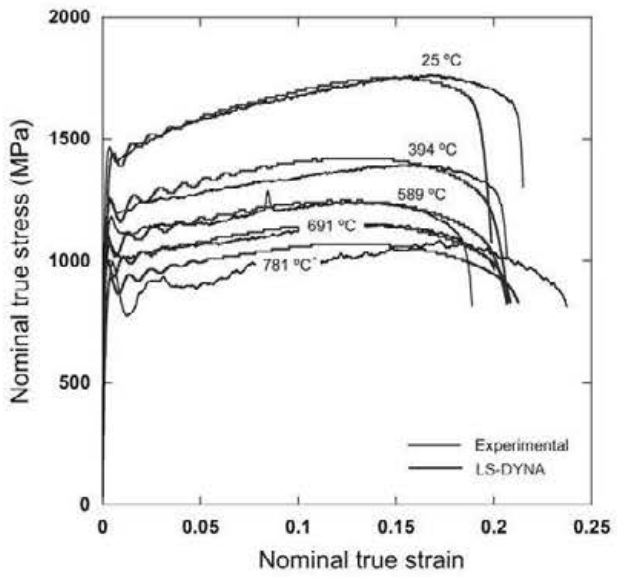

Fig. 7. True nominal stress–strain curves of the tensile tests at various temperatures performed at a strain rate of $1.0 \times 10^3\ s^{-1}$ compared with the numerical simulations.

where ε_i is the strain corresponding to the incident wave, ε_r is the strain of the reflected wave and ε_t is the strain of the transmitted wave. The specimen engineering stress s is:

$$s = \frac{F_s}{A_0} = \frac{E_b A_b}{A_0}\varepsilon_t \tag{4.2}$$

where F_s is the force applied over the specimen by the SHTB, E_b is the elastic modulus of the input and output bars and A_b is the input and output bar cross-section area. The specimen engineering strain e and strain rate $\dot{e}$ are:

$$e = -\frac{2c_0}{l_s}\int_0^t \varepsilon_r dt \tag{4.3}$$

$$\dot{e} = -\frac{2c_0}{l_s}\varepsilon_r \tag{4.4}$$

where $c_0 = \sqrt{E_b/\rho_b}$ is the elastic wave propagation velocity inside input and output bars, ρ_b is the mass density of the bars and l_s is the specimen initial length.

Assuming the volume conservation, the well-known expressions for the determination of the nominal true stress and true strain from their corresponding engineering values (Lubliner, 1990) can be used. The expressions are as follows:

$$\varepsilon_N = \ln(1+e); \quad \sigma_N = s(1+e) \tag{27}$$

The sub-index "N" was used to distinguish them from the true stress and strain calculated with the current diameter measurements (see Eqs. (23) and (24)). According to that stated in the previous section, the initial stress triaxiality was $\sigma^* = 1/3$, whereas the Lode angle was $\theta = -30°$ (see Table 3).

The diameter of the fractured specimens was measured by employing an optical profilometer. Those values of the diameters allowed calculating the equivalent plastic strain to failure values as:

$$\bar{\varepsilon}_p^f = 2\ln\left(\frac{d_0}{d_f}\right) \tag{28}$$

The true nominal stress–strain curves for the axisymmetric smooth specimens tested at various temperatures are gathered in Fig. 7. A progressive decrease of the strength with the temperature was clearly observed. The flow stress at 0.5% of the equivalent plastic strain (solid blue[1] circles) and equivalent plastic strain to failure (solid red squares) are plotted against the natural logarithm of the dimensionless strain rate and the homologous temperature in Fig. 8(a) and (b), respectively. The former figure shows that both flow stress and equivalent plastic strain to failure grew with the strain rate, while the latter shows a decrease of the flow stress and an increase of the equivalent plastic strain to failure with the temperature.

4.3. Quasi-static tests of plane specimens

The quasi-static tensile tests of plane specimens were carried out by using a screw-driven universal testing machine. The tests were conducted at a strain rate of $1.0 \times 10^{-3}\ s^{-1}$. Two geometries, corresponding to two different stress states, were utilised. The geometry and dimensions of the shear and the plane strain specimens can be seen in Fig. 9(a) and (b), respectively. Both geometries were machined from 1.6 mm thickness plates. The geometries presented here, have been previously employed in the calibration of Lode angle dependent models by Gruben et al. (2012).

The gauge area of the shear specimens is especially designed to develop a pure shear stress state. Therefore, the initial values for the triaxiality and Lode angle assuming a pure shear stress state in the gauge area, are $\sigma^* = 0$ and $\theta = 0°$.

As pointed out by Gruben et al. (2011), the small length-width ratio of the gauge area in the plane strain specimens yields a nearly plane strain stress state. Assuming plane strain state, the equivalent stress in terms of principal stresses is:

$$\bar{\sigma} = \sqrt{\frac{1}{2}3\left(\frac{1}{2}\sigma_1\right)^2} = \frac{\sqrt{3}}{2}\sigma_1 \tag{29}$$

and the hydrostatic stress is given by:

$$\sigma_H = 1/2\sigma_1 \tag{30}$$

The initial triaxiality and Lode angle values for the plane strain specimen are $\sigma^* = 1/\sqrt{3} \approx 0.577$ and $\theta = 0°$.

The tests were recorded by using a high-resolution digital camera. The images acquired by the camera were post-processed employing an in-house Digital Image Correlation (DIC) software programmed by Fagerholt et al. (2010). One side of the plane specimens was painted in white and sprayed with black paint afterwards to create a speckle pattern (see Fig. 10 (a) and (b)). This speckle pattern allowed the DIC software to obtain the strain fields in the gauge area of the specimens. Additionally, an extensometer with 20 mm of gauge length was attached to the specimens.

The load–displacement curves of the quasi-static tensile tests of the shear and plane strain specimens are plotted in Fig. 11(a) and (b), respectively. The equivalent strain to failure was measured in the most critical zone of the gauge area in both specimen geometries, i.e. in the centre of the gauge areas.

5. Identification of constants

The identification of constants process for elastoplastic-damage coupled material models is iterative by nature, since constitutive relation is fed by the failure criterion. It can be a tough process if the starting point for the iterative procedure is not carefully chosen. The numerical simulations of the tests were an essential tool for the calibration procedure. The JXCd material model was implemented in LS-DYNA (2007) non-linear finite element commercial code by means of a user-defined material subroutine. The time integration was chosen explicit The element erosion was

[1] For interpretation of colour in Figs. 1, 2, 4, 5, 7, 8 and 10–20, the reader is referred to the web version of this article.

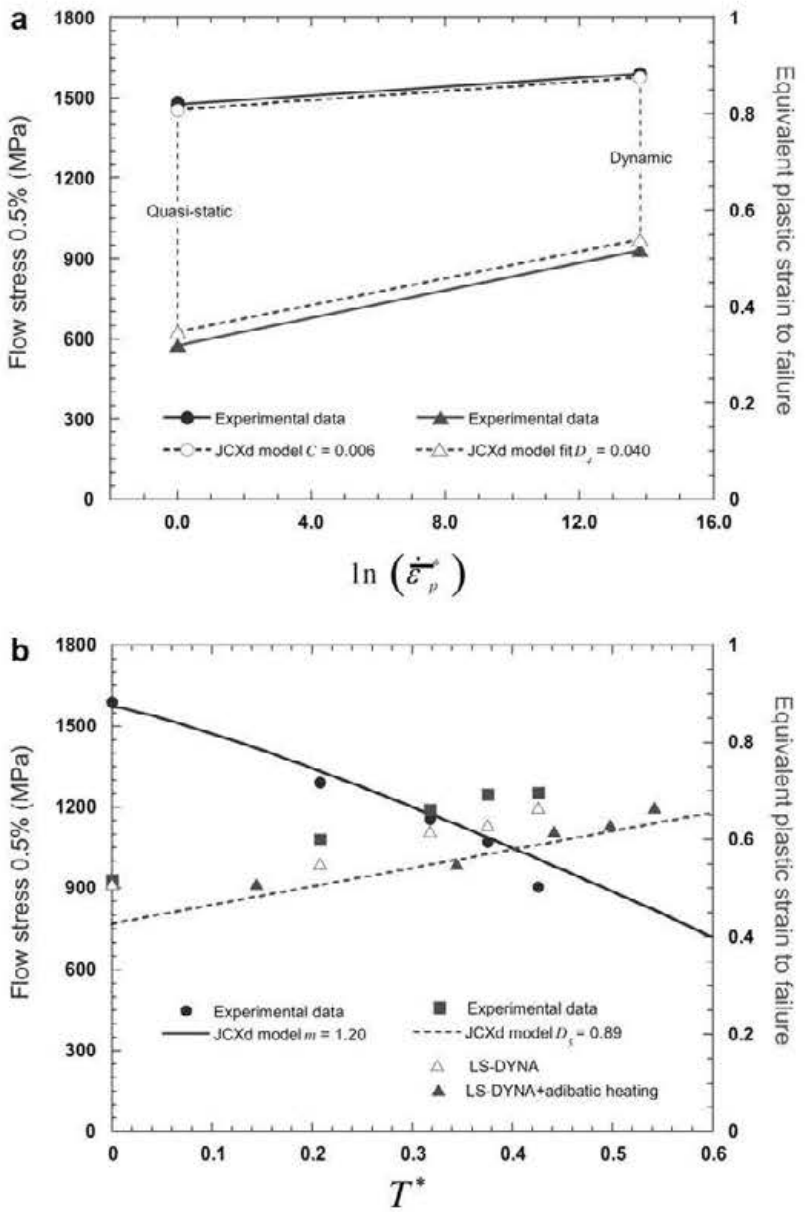

Fig. 8. (a) Flow stress at $\bar{\varepsilon}_p = 0.05$ and experimental values of the equivalent plastic strain to failure against the natural logarithm of the dimensionless strain rate ($\ln(\dot{\bar{\varepsilon}}_p^*)$). (b) Flow stress at $\bar{\varepsilon}_p = 0.05$ and experimental and numerical values of the equivalent plastic strain to failure against the temperature.

performed setting the stress tensor equal to zero, $\boldsymbol{\sigma} = \mathbf{0}$, when the damage parameter reached the unity, $D = 1$. All the simulations were carried out without mass scaling. More details on the implementation are given in Erice (2012). The calibration procedure was ordered in four stages. In each one of these stages a set of constants was calibrated.

5.1. Determination of A, B, n, D_1, D_2, D_3 and the weakening exponent β

In this stage the quasi-static tests of axisymmetric smooth and notched specimens were used. The specimens were modelled by using eight-node solid elements with one integration point and stiffness-based hourglass control. Forty-four elements across the diameter were employed in the gauge area, giving an approximate element size of $68 \times 68 \times 68\ \mu m^3$ (see Fig. 12(a)–(c)). A prescribed motion was imposed to the nodes corresponding to one end of the specimen, while the movement of the nodes corresponding to the opposite end were also constrained. The numerical simulations were run with quasi-static loading conditions. The minimum cross-section diameter was monitored in order to determine the true strain.

An initial set of constants was necessary to start the iterative process. As a first approximation, no weakening was assumed, this is, $\beta^0 = \infty$ (see Fig. 13). The Johnson–Cook type damage evolution law was adopted since there was not any experimental evidence found that suggested any other behaviour. Therefore, the material parameter m_D was set $m_D = 1.0$ yielding to the next damage evolution law:

$$\dot{D} = \frac{1}{\bar{\varepsilon}_p^{fJCXd}(\sigma^*, \dot{\bar{\varepsilon}}_p, T, \theta)}\dot{\bar{\varepsilon}}_p$$
$$H_2 = \frac{1}{\bar{\varepsilon}_p^{fJCXd}(\sigma^*, \dot{\bar{\varepsilon}}_p, T, \theta)} \tag{31}$$

The initial values for the failure criterion constants D_1^0, D_2^0 and D_3^0, were obtained by fitting the failure locus curve on the equivalent plastic strain to failure vs. triaxiality space using Bridgman's analysis (Børvik et al., 2001). The initial triaxiality and the

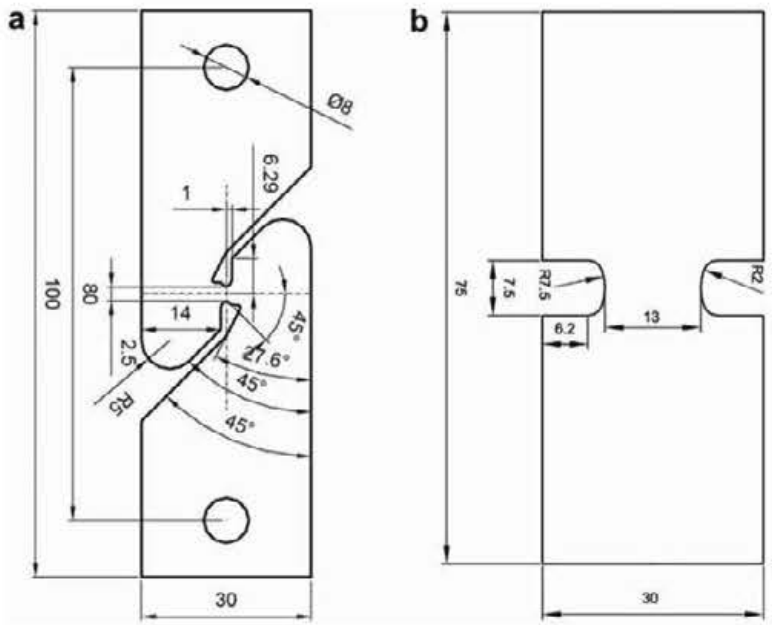

Fig. 9. Dimensions and geometry of the 1.6 mm thickness plane specimens: (a) shear specimen and (b) plane strain specimen.

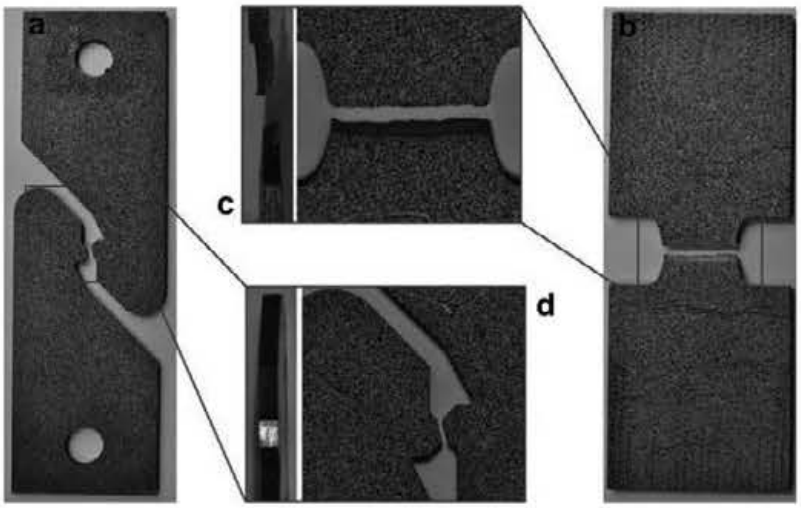

Fig. 10. Plane specimens painted with a speckle pattern. (a) Shear and (b) plane strain specimens after fracture. (c,d) show in detail the fracture area of plane strain and shear specimens, respectively.

experimental equivalent plastic strain to failure values used for such a fit are listed in Table 3. The strain rate dependency was ignored by setting $C^0 = D_4^0 = 0$, and the thermal softening was deactivated setting the Taylor–Quinney constant equal to zero, $\chi^0 = 0$. The Lode angle dependency was also deactivated by setting $\gamma_F^0 = 1$.

The initial values of A^0, B^0 and n^0 were determined with the experimental true stress–plastic strain curve plotted in Fig. 4(b). A, B and n were adjusted with a certain amount of simulation runs of the smooth axisymmetric specimen until the stress–plastic strain response obtained fitted the experimental one (see Table 4).

Having fixed A, B and n with the set of initial constants D_1^0, D_2^0 and D_3^0, numerical simulations of the three axisymmetric specimens were run. The purpose of such simulations was to obtain a first approximation of the triaxiality and equivalent plastic strain histories. It has been proven (Børvik et al., 2003, 2005; Erice et al., 2012) that the triaxiality ratio in the centre of axisymmetric specimens is far from being constant during tensile tests. Therefore, the triaxiality histories were collected and averaged from the centre of the specimens, while the equivalent plastic strains were computed as $\bar{\varepsilon}_p = 2\ln(d_0/d)$ in order to compare it with the experimental values. With those corrected values a new set of D_1^1, D_2^1 and D_3^1 was determined.

The weakening exponent was calibrated only by employing the true-stress strain curve of the smooth axisymmetric specimen. A constant value of $\bar{\varepsilon}_p^{f\,JCXD} = D_1^1 + D_2^1 \exp(1/3D_3^1) \approx 0.5$ was assumed for the estimation of the weakening exponent β. Otherwise, the calculation of the weakening function would not be trivial task. The effect of the weakening exponent β on the constitutive relation $Y^{JCXD} = (1 - D^\beta)(A^0 + B^0\bar{\varepsilon}_p^{n^0})$ is plotted in Fig. 13. After a few simulation runs, the value $\beta = 6.0$ was chosen as a good value for the weakening exponent. Once the constants of the damage evolution and weakening function were fixed, $m_D = 1.0$ and $\beta = 6.0$, several

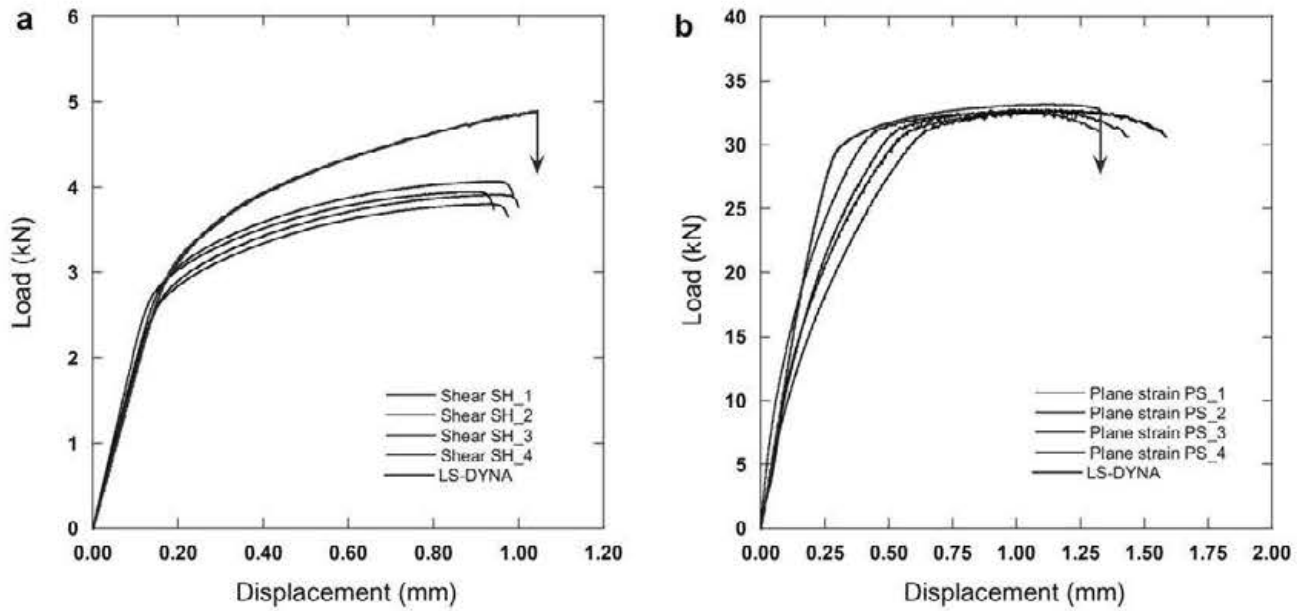

Fig. 11. Load–displacement curves of the (a) shear and (b) plane strain specimens tested at a strain rate of $1.0 \times 10^{-3}\,s^{-1}$ compared with the numerical simulations.

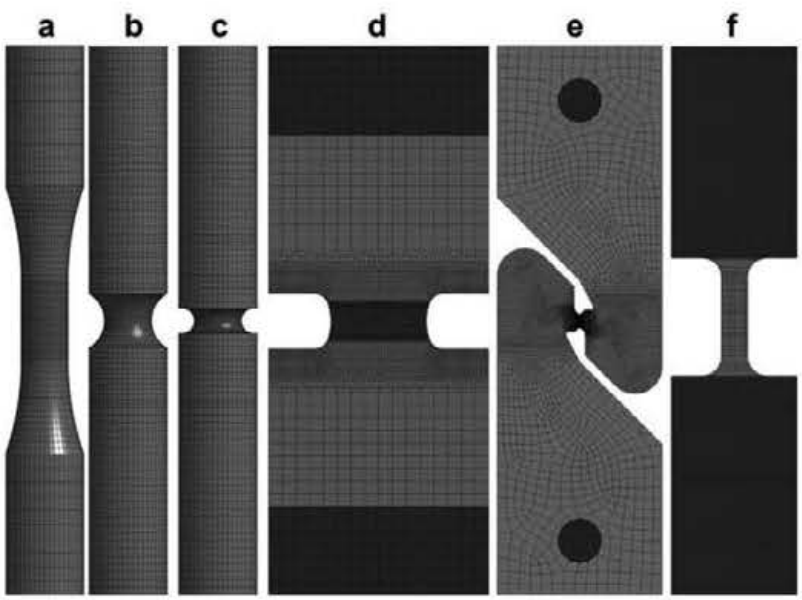

Fig. 12. Meshes of the finite element models employed to carry out the numerical simulations of the mechanical tests. Smooth axisymmetric specimen (a), notched axisymmetric with notch radii $R = 2$ mm (b) and $R = 0.8$ mm (c), shear specimen (d), plane strain specimen (e) and SHTB with a smooth axisymmetric specimen (f).

simulations of the three axisymmetric specimens were run modifying D_1^k, D_2^k and D_3^k until the best fit with the experimental results was obtained.

The equivalent plastic strain to failure expression of the JCXd model as a function of the triaxiality is plotted in Fig. 14(a) as a black solid curve. It should be mentioned that such a curve is for values with constant Lode angle of $\theta = -30°$, therefore $\mu_\theta = 1.0$. The dashed green lines show the evolution of the equivalent plastic strain as a function of the triaxiality during the loading until failure for the axisymmetric specimens. The failure is marked with green solid circles.

5.2. Determination of γ_F

Numerical simulations of the plane specimens were performed in the present calibration stage. The finite element models of the shear and plane strain specimens are shown in Fig. 12(d) and (e), respectively. The red coloured parts in Fig. 12 were modelled as rigid bodies.

In the shear finite element model, the red coloured parts simulate the bolts that transmitted the load from the testing machine to the specimens (see Fig. 12(d)). In the in-plane gauge area, an approximate element size of $60 \times 60\ \mu m^2$ was used. Eight elements were employed to discretise the thickness. In order to avoid element volumetric locking in the gauge area, eight-node fully integrated solid elements were used, while in the rest of the specimen eight-node solid elements with one integration point were employed. Prescribed motions were imposed to the rigid bodies that simulating quasi-static loading conditions.

The red parts of the plane strain finite element model represent the clamps that held the specimens during the tests (see Fig. 12(e)). The in-plane gauge area was meshed with an approximate element

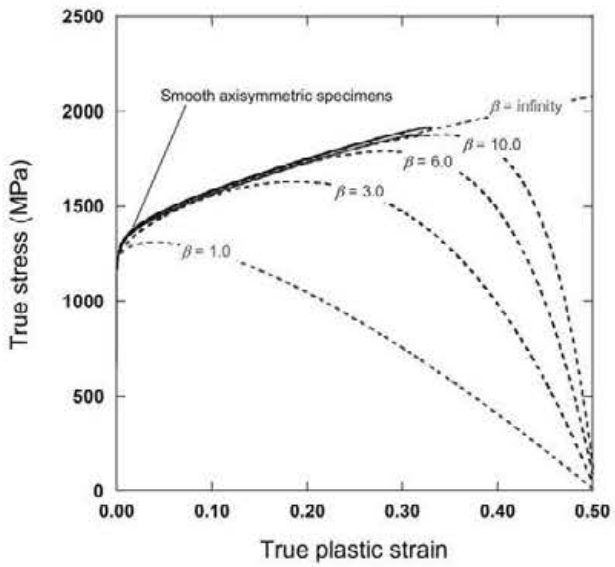

Fig. 13. Effect of the weakening exponent on the constitutive relation of the JCXd material model for precipitation hardening Inconel 718 nickel-base superalloy.

size of $80 \times 80\ \mu m^2$. The thickness was discretised with eight elements. Eight-node solid elements with one integration point and stiffness-based hourglass control were used for the whole finite element model of the plane strain specimen. The quasi-static loading conditions were simulated imposing prescribed axial motions to the rigid bodies.

The displacement was computed in both shear and plane strain specimens by monitoring the axial displacement of two nodes that simulated the initial gauge length of the extensometer. The triaxiality and equivalent plastic strain histories were collected from elements that coincided with the points from where the DIC measurements were performed.

The only constant to be calibrated in this stage was γ_f. With the calibrated constants of D_1, D_2 and D_3 the equivalent plastic strain to failure for the initial values of triaxiality and Lode angle corresponding to the pure shear stress state ($\sigma_0^* = 0$ and $\theta = 0°$) gave $\bar{\varepsilon}_p^{fJCXD} = (D_1 + D_2) \cdot \gamma_f \approx 0.81 \cdot \gamma_f$. A starting value was set for γ_f based on the experimental equivalent plastic strain to failure of the pure shear stress state:

$$\gamma_f = \bar{\varepsilon}_p^{f\,5\,\exp} / \bar{\varepsilon}_p^{f\,T}(\sigma^* = 0, \theta = 0°) = 1.1/0.81 \approx 1.36 \tag{32}$$

After performing a certain amount of simulation runs $\gamma_f = 1.50$ was found to be a good value for such a constant. Fig. 14(a) shows in green dashed lines the equivalent plastic strains collected from the above-mentioned elements as a function of the triaxiality until failure, marked with solid green triangles. In the same figure, the black solid curve corresponds to the calibrated equivalent plastic strain to failure expression of the JCXd model for $\mu_\theta = 1.0$, whereas the red solid curve corresponds to the calibrated expression for $\mu_\theta = 1.5$. The Lode angle dependent function is plotted in the $\varepsilon_1 + \varepsilon_2 + \varepsilon_3 = 0$ plane in the principal strain space in Fig. 15.

5.3. Determination of C, D_4, m and D_5

Numerical simulations of the dynamic tensile tests of axisymmetric smooth specimens were performed in this stage of the calibration procedure. The finite element model used for the simulation of such tests is depicted in Fig. 12(f). Twenty elements across the diameter, giving an approximate element size of $150 \times 150 \times 150\ \mu m^3$, were used. The discretisation was performed employing eight-node solid elements with one integration point and stiffness-based hourglass control.

The incident wave was simulated as a prescribed velocity in the nodes of the input bar end nodes. The incident stress wave was transform to a velocity profile with $v(t) = c_0 \varepsilon_i(t)$. The incident, reflected and transmitted stress waves were collected from element on the periphery of the input and output bars, located at the same distance as the strain gauges of the SHTB (see Fig. 6).

The constant C was obtained fitting linearly the flow stresses at 0.5% equivalent plastic strain of quasi-static and dynamic tests at room temperature (see Fig. 8(a)). The 0.5% equivalent plastic strain value was chosen to avoid the oscillations that appear at low strains in the dynamic true nominal stress–strain curves (see Fig. 7). Avoiding such oscillations means that the flow stress was measured ensuring that the specimen was being strained at constant strain rate, i.e. the specimen was in equilibrium. The model can be expressed only as a function of the dimensionless strain rate as follows:

$$Y_{0.5\%}^{JCXd}(\dot{\bar{\varepsilon}}_p^*) = (1 - \cancel{\Omega}^\beta)[A + B(0.05)^n][1 - C \ln(\dot{\bar{\varepsilon}}_p^*)][1 - \cancel{T}^{*m}] \tag{33}$$

where the weakening and the thermal softening effect are considered negligible due to the low equivalent plastic strain. Fig. 8(a) shows the fitting of model and experimental data.

$D_4$was similarly adjusted, the equivalent plastic strain to failure values of the quasi-static and dynamic tests at room temperature were compared. The equivaelent plastic strain to failure expression of the JCXd model may be written as a function of the dimensionless strain rate as:

$$\bar{\varepsilon}_p^{fJCXd}(\dot{\bar{\varepsilon}}_p^*) = [D_1 + D_2 \exp(D_3 \cdot 0.615)][1 + D_4 \ln(\dot{\bar{\varepsilon}}_p^*)] \tag{34}$$

The triaxiality value was computed from the quasi-static tensile tests as is specified in Section 5.1. Fitting linearly the data D_4 was obtained (see Fig. 8(a)). It should be noted that the triaxiality changed for the dynamic tests, as is going to be showed later on in the article. Additionally, the temperature of the specimen increased during the dynamic loading due to adiabatic heating. Therefore, the D_4 constant was validated simulating the tensile test carried out in the SHTB. Using the same approach as in Section 5.1, the triaxiality and equivalent plastic strain histories were gathered from the numerical simulations. The experimental and numerical equivalent plastic strain to failure values were in good agreement as can be seen in Table 3.

The thermal softening exponent m was obtained by comparing the flow stresses at 0.5% of the equivalent plastic strain for the dynamic tests carried out at various temperatures. Now, the constitutive relation of the JCXd material model can be written as a function of the homologous temperature as:

$$Y_{0.5\%}^{JCXd}(T^*) = (1 - \cancel{\Omega}^\beta)[A + B(0.05)^n][1 - C \ln(10^6)][1 - T^{*m}] \tag{35}$$

Fig. 8(b) depicts the evolution of the normalised flow stresses with the homologous temperature as well as the JCXd model fit with $m = 1.20$. Note that for such a low equivalent plastic strains the adiabatic heating does not affect at the flow stress measurement.

Nevertheless, the adiabatic heating plays and important role in the determination of D_5. The Fig. 8(b) shows the experimental equivalent plastic strains to failure of the dynamic tests performed at various temperatures plotted in solid red squares. However, the temperature increment could not be measured in the test. Typically, such an increment is measured as:

$$\Delta T = \frac{\chi}{\rho C_p} \int_0^{\bar{\varepsilon}_p^f} \bar{\sigma} d\bar{\varepsilon}_p \tag{36}$$

In this study the equivalent stress–strain curves for the dynamic tests were not calculated. To obtain such curves, in-situ minimum cross-section diameter measurements (Arthington

Table 4
JCXd material constants for precipitation hardened Inconel 718.

Physical properties and isotropic elastic constants							
E (GPa)	ν	ρ (kg/m^3)	C_p (J/kg °C)	χ			
185	0.33	8190	435	0.9			
Constitutive relation							
Strain hardening			Strain rate hardening		Thermal softening		
A (MPa)	B (MPa)	n	C	$\dot{\varepsilon}$ (s^{-1})	m	T_r (°C)	T_m (°C)
1200	1284	0.54	0.006	1.0×10^{-3}	1.20	25	1800
Failure criterion							
D_1	D_2	D_3	D_4	D_5			
0.04	0.75	−1.45	0.04	0.89			
Weakening constants and Lode angle dependence							
β	m_D	γ_F	k				
6.00	1.00	1.50	1.00				

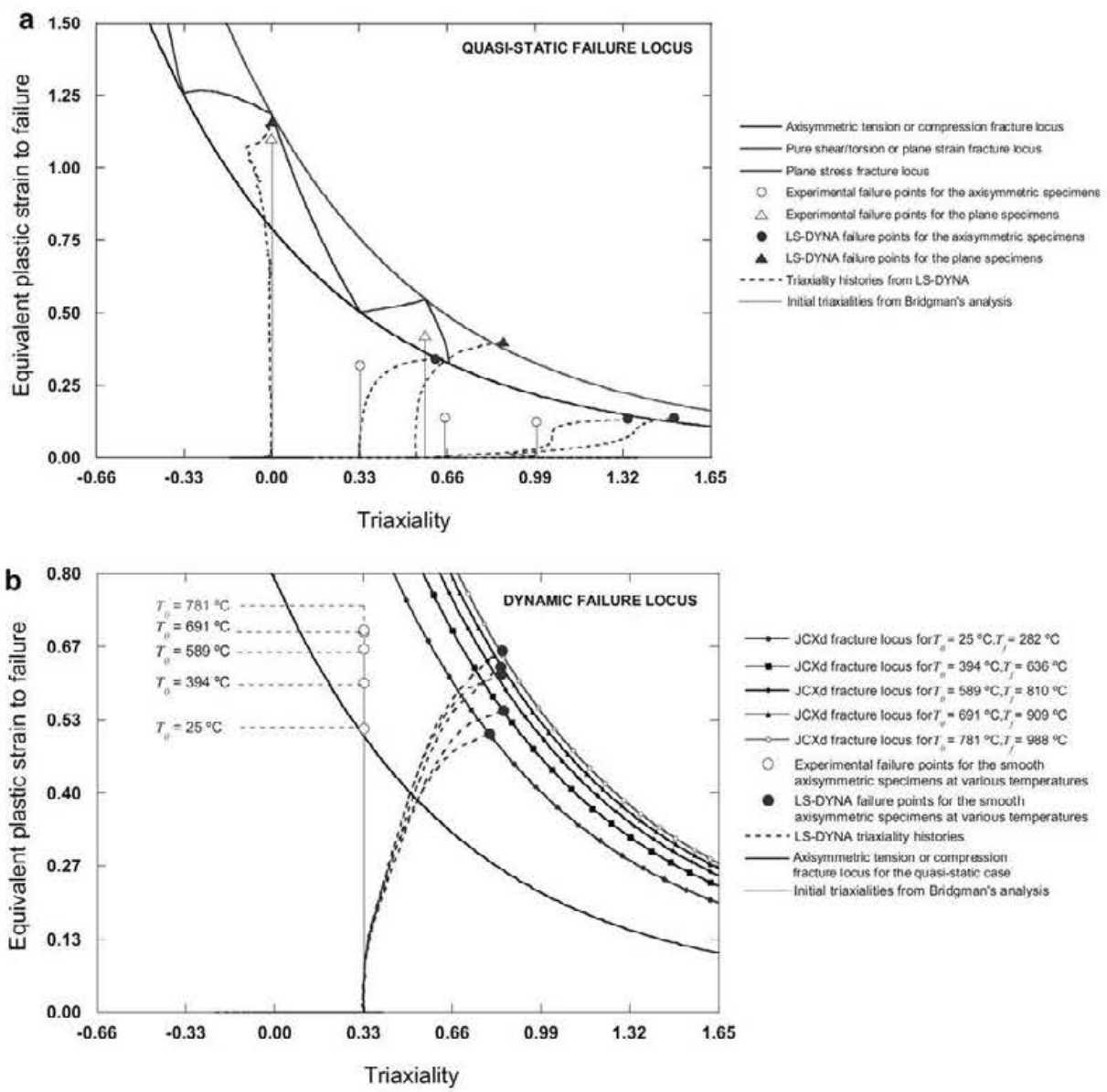

Fig. 14. Fracture loci in the equivalent plastic strain vs. triaxiality space for the (a) quasi-static and (b) dynamic loading cases.

et al., 2012; Arthington et al., 2009) and a true stress correction based on the notch curvature radius (Bridgman, 1952; Le Roy et al., 1981; Mirone and Corallo, 2010) are required. To cope with this issue and be consistent with the calibration methodology, a more local measurement was taken. The adiabatic temperature increment was computed and averaged for the same elements from which the triaxiality was obtained. The temperature and the triaxiality values at failure collected from such elements are reported in Table 3. The equivalent plastic strains to failure computed from the numerical simulations are shown in Fig. 8(b) as hollow red triangles. The same values are plotted in solid red triangles after summing the adiabatic heating to their initial temperatures. Now the equivalent plastic strain to failure of the JCXd model for dynamic tests can be written as a function of the homologous temperature as:

$$\bar{\varepsilon}_p^{f\,JCXd}(T^*) = [D_1 + D_2 \exp(D_3 \cdot 0.80)][1 + D_4(10^6)][1 + D_5(T^*)] \quad (37)$$

Although the triaxiality changes for different temperatures, it should be noted it was maintained constant, $\sigma^* = 0.8$ when plotting the model (dashed red line). The constant D_5 was obtained fitting the data shown in Fig. 8(b).

5.4. Fracture locus

The JCXd material model constants calibrated for the precipitation hardening Inconel 718 nickel-base superalloy are listed in Table 4. The calibrated fracture locus in the equivalent plastic strain vs. triaxiality space for the quasi-static case is plotted in Fig. 14(a). In the figure, the black solid curve corresponds to the axisymmetric tension or compression stress state failure locus ($\theta = -/+30°$, $\mu_\theta = 1.0$), whereas the red solid curve corresponds to the pure shear/torsion or plane strain states failure locus ($\theta = 0°$, $\mu_\theta = 1.5$). The blue solid curve represents the failure locus of the plane stress state. For such a stress state the Lode angle is not constant, it is a function of the stress triaxiality as (Erice, 2012; Walker, 2013):

$$\theta(\sigma^*) = -\frac{1}{3}\sin^{-1}\left\{-\frac{27}{2}\sigma^*\left[(\sigma^*)^2 - \frac{1}{3}\right]\right\} \quad (38)$$

That is why the blue solid curve shows local minimum and maximums in the equivalent plastic strain vs. triaxiality space (see Fig. 14(a)). The three dimensional fracture surface plotted in Fig. 16 shows the same "zigzag" shaped blue curve.

In Figs. 14(a) and 16 the hollow points, circles and triangles, are plotted using the experimental equivalent plastic strain to failure and the constant initial triaxiality calculated with the Bridgman's analysis. The constant triaxiality loading path is plotted in solid green lines. Conversely, the dashed green curves show the evolution equivalent plastic strain while the specimens are being loaded until failure obtained from the numerical simulations of the axisymmetric specimens. The failure is marked with solid green points, circles and triangles. The Lode angle and triaxiality histories were collected from the centre of the specimens, whereas the equivalent plastic strain was computed employing the current minimum cross-section diameter measurements. For the shear and plane strain specimens the equivalent plastic strain, Lode angle and triaxiality histories were taken from elements close to the points from where DIC measurements were performed. Fracture initiation in the plane specimens was detected in the interior and not in the surface. Hence, the elements from which the histories were collected were the interior elements.

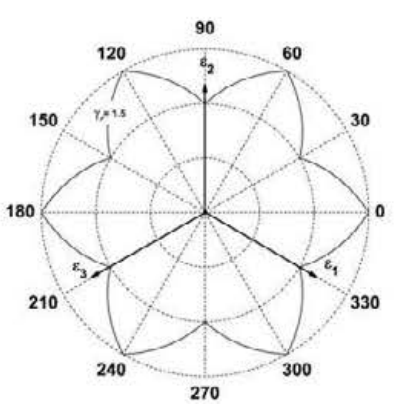

Fig. 15. Second kind of Lode angle dependent function for $\gamma_f = 1.5$ plotted in the $\varepsilon_1 + \varepsilon_2 + \varepsilon_3 = 0$ plane of the principal strain space for constant triaxiality.

The fracture loci for various temperatures and constant strain rate are depicted in Fig. 14(b). In order to compare the fracture loci at low and high strain rates, the fracture locus for the quasi-static case was also plotted in the figure as a solid black curve. The figure shows in dashed green curves the triaxiality-dependent path that the equivalent plastic strain followed during the dynamic loading for various temperatures until failure, marked with green solid circles. To construct such paths numerical simulations were necessary, the triaxility and temperature histories were collected from the elements located in centre of the specimens. The current minimum cross-section diameter measurements were employed to compute the equivalent plastic strain. The solid green lines and hollow green circles represent the constant initial triaxility and experimental strain to failure at various temperatures, respectively.

In all the studied cases, the equivalent plastic strain histories collected from the simulations started from their corresponding initial, or analytical, triaxiality values though they soon left to be constant. Therefore, the numerical simulations were necessary to calibrate the failure criterion. As pointed out in by Erice et al. (2012), the Bridgman's analysis only could work as a lower limit for the failure criterion. The triaxiality, Lode angle and equivalent plastic strain to failure for all the cases are summarised in Table 3.

6. Numerical study

6.1. Results

The objective of this study was to check the capability of the calibrated JCXd material model (see Table 4) to predict the true stress–strain and load–displacement experimental curves. The strain corresponding to the specimens failure was also analysed. All the numerical simulations were run with the same discretisations as those employed in the calibration procedure.

The true stress–strain curves obtained from the numerical simulations of the quasi-static tensile tests at room temperature corresponding to the smooth and notched specimens with notch radius $R = 2.0$ mm and $R = 0.8$ mm are shown in Fig. 4(a). The true stress–strain curves of the smooth axisymmetric and $R = 2.0$ mm notched specimens were in excellent agreement with the experimental data. Both elastoplastic behaviour and failure strains, marked with blue arrows, were quite well predicted (see Table 3). Nevertheless, observing Fig. 4(a), one can see that the elastoplastic response was slightly overestimated for the $R = 0.8$ mm notched axisymmetric specimen. This seems to be a generalised issue since has been reported in several studies (Børvik et al., 2003, 2005; Dey et al., 2006). The failure was also higher than the experimental value as can be also observed in Fig. 14(a). However, the model was considered to give reliable results.

The comparison between the experimental and numerical true nominal stress–strain curves of the dynamic tensile tests at various

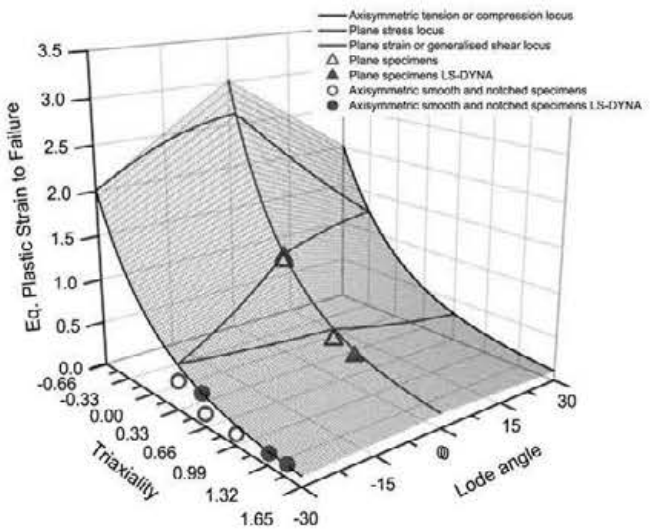

Fig. 16. Fracture surface of the postulated material model corresponding to quasi-static loading case.

temperatures is depicted in Fig. 7. The numerical results seem to be predicting the elastoplastic behaviour with reasonable accuracy for temperatures ranging from 25 °C to 691 °C. Nevertheless, the numerical true nominal stress–strain curve of the highest initial temperature was above the experimental response. This result was expected since the model fitting was also slightly above the experimental flow stress at 0.5% of equivalent plastic strain as can be seem in Fig. 8(b). The equivalent plastic strain to failure was found reasonable for all the temperatures. The experimental and numerical equivalent plastic strains to failure are reported in Table 3.

The numerical load–displacement curve is compared with the experimental register for the tensile tests of the shear specimens in Fig. 11(a). The load–displacement response is overestimated by the numerical simulations. A plausible reason for that behaviour is that the plates, from which the plane specimens were machined, were manufactured by rolling. Fourmeau et al. (2011), obtained a very similar behaviour when testing aluminium plates with the same geometry. They reported that such behaviour might be due to the anisotropy of the rolled plates. In the present case, the grain texture could have been the responsible of the overestimation of the elastoplastic behaviour. Additionally, the load–displacement curves obtained for the different specimens presented a considerable scatter. Conversely, the strain to failure was in close agreement with the experimental data (Table 3). A DIC image from a representative test is compared with the numerical simulation of the shear specimen in Fig. 17, where equivalent plastic strain contours can be seen. Both, DIC and numerical simulation, presented the same equivalent plastic strain contours and they were localised in the same zone. The load–displacement curve from the numerical simulation of the plane strain specimens is plotted in Fig. 11(b). The elastoplastic response as well as the failure strain were reasonably predicted.

6.2. Mesh sensitivity study

The fracture patterns for three test types were studied in Chocron et al. (2011). The mesh size was found to be crucial for obtaining the desired patterns. In this research, the capability of the JCXd material model to predict complex fracture patterns was analysed.

A cup-cone fracture pattern was expected when simulating the axisymmetric smooth specimens. However, the mesh size used for the calibration of the model was not able to capture such a pattern. The damage contours for the simulations run with 44 elements across the diameter are plotted in the first sequence of Fig. 18. A flat fracture surface was obtained. However, the damage contours indicated that a slanted localisation existed near the perimeter of the specimen when the crack was expanding outwards. The next numerical simulation was performed by using 72 elements across the diameter. The fracture sequence can be seen in the second row of the Fig. 18. On this occasion, the suspicions were confirmed. Localisation, while more obvious, was not able to form slanted fractures. Nevertheless, the fracture pattern obtained was not flat any more. The fracture surface was a mixture between the flat surface and cup-cone. Finally, a numerical simulation with 144 elements across the diameter was carried out. The last row of stacked images from Fig. 18 shows the fracture sequence. The localisation near the border produced the expected slanted fracture shaping a cup-cone fracture pattern. A smaller mesh size than the used in the JCX model (Chocron et al., 2011) was necessary to capture the cup-cone fracture pattern.

The fracture pattern of the shear specimen (see Fig. 10(d)) was predicted with the mesh used in the calibration procedure of the material model. Since the plastic strain was extremely localised almost from the moment that the plasticity appears in the specimen, is not a complex pattern to predict (see Fig. 17).

The plane strain specimens presented a slanted fracture pattern as can be seen in Fig. 10(c). The same patterns have been reported previously by Besson et al. (2001) or Xue (2009). The numerical simulation carried out with the model calibration mesh that had eight elements over the thickness, gave a flat fracture surface. In order to see the fracture initiation in the images collected from the numerical simulations, half of the specimen was removed (see Fig. 19).

A sequence showing three images: intact, fractured and fully fractured, was obtained to study the effect of the mesh size on the fracture pattern of the plane strain specimens. The fracture sequence is plotted with damage contours in the first row of the Fig. 19. Damage localisation was clearly observed in "X-like" shape but the elements were too big to take it into account. The element

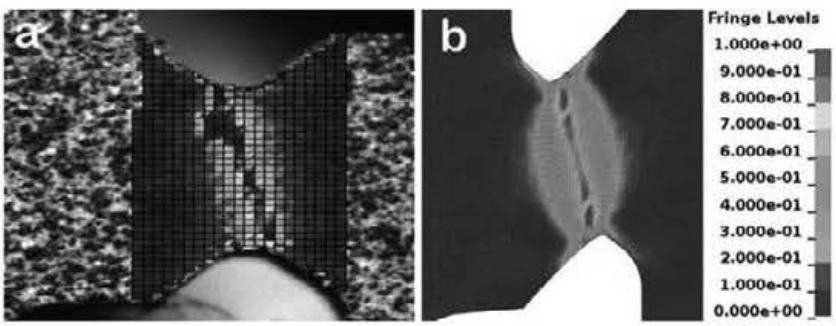

Fig. 17. DIC strain field (a) from a representative shear specimen compared with the numerical simulations (b) just before failure occurred.

refining was only performed in the thickness direction of the specimen. The in-plane discretisation was much finer than the discretization made in the thickness direction. Therefore, it was considered that changing the element size in the thickness direction will give reasonable results.

In the first refinement, 16 elements were used over the thickness. Even though, the localisation seemed to be stronger, the same result as the coarsest mesh was obtained. The fracture sequence can be seen in the second row of Fig. 19. Finally, 32 elements over the thickness were employed to mesh the specimen. With this element size the slanted fracture appeared in the centre of the specimen, as can be observed in the last row of stacked images in Fig. 19.

6.3. Lode angle dependency

To ensure that the fracture patterns obtained in the precious section (cup-cone and slanted fracture) were not obtained as a result of the discretisation, the effect of the weakened constitutive equations and the Lode angle in such pattern prediction was studied. To form an idea of the importance that the weakening and the Lode angle had in the fracture prediction, three cases were run for both smooth axisymmetric and plane strain specimens with the finest mesh discretisation. This is, 144 elements were used across the diameter for the smooth axisymmetric specimen and 32 elements over the thickness for the plain strain specimen. The cases run were all particular cases of the proposed JCXd material model (the reader is referred to Section 2 for the formulation details):

(i) No weakening and no Lode angle dependency. This was a regular uncoupled Johnson–Cook material model. To uncouple the constitutive equations the weakening exponent was set to $\beta = \infty$. The Lode angle dependency was deactivated from the failure criterion making $\gamma = 1.0$, which led to a constant value of the Lode angle dependent function of $\mu_\theta = 1.0$.

(ii) No weakening but Lode angle dependent failure criterion. Which is equivalent to a Johnson–Cook-like uncoupled constitutive relationship with a Lode angle dependent failure criterion. Again, the model was uncoupled setting $\beta = \infty$. In contrast to the case (i), here the failure criterion used the calibrated value of $\gamma = 1.5$ for the Lode angle dependent function (see Table 4).

(iii) Weakened constitutive equations and Lode angle dependent failure criterion, or JCXd coupled material model. The calibrated weakening exponent $\beta = 6.0$ was employed, i.e. the coupled elastoplastic-damage constitutive equations were activated. As occurred in case (ii) the calibrated value of $\gamma = 1.5$ was used for the Lode angle dependent function (see Table 4).

The results obtained after running the numerical simulations for the axisymmetric specimen for the three cases (i), (ii) and (iii)

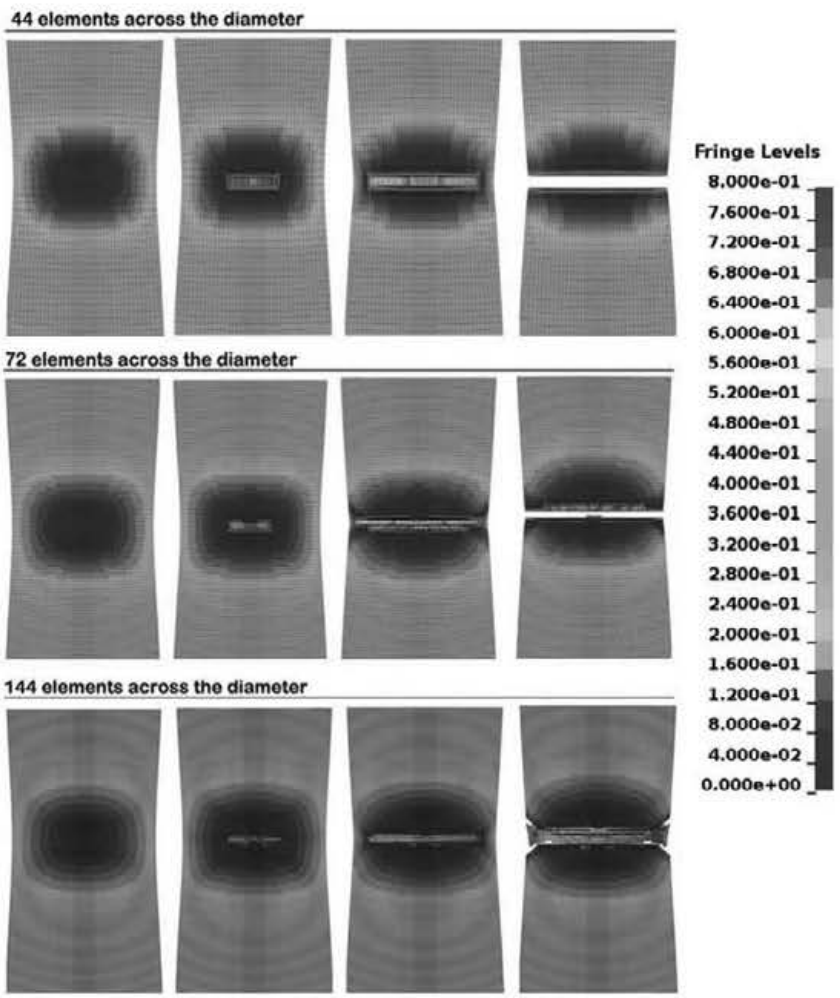

Fig. 18. From left to right, numerical simulations of the fracture sequence on smooth axisymmetric specimens depending on the element size. The last images of the sequences show the mesh size sensitivity of the cup-cone fracture pattern. Damage contours are plotted in the images.

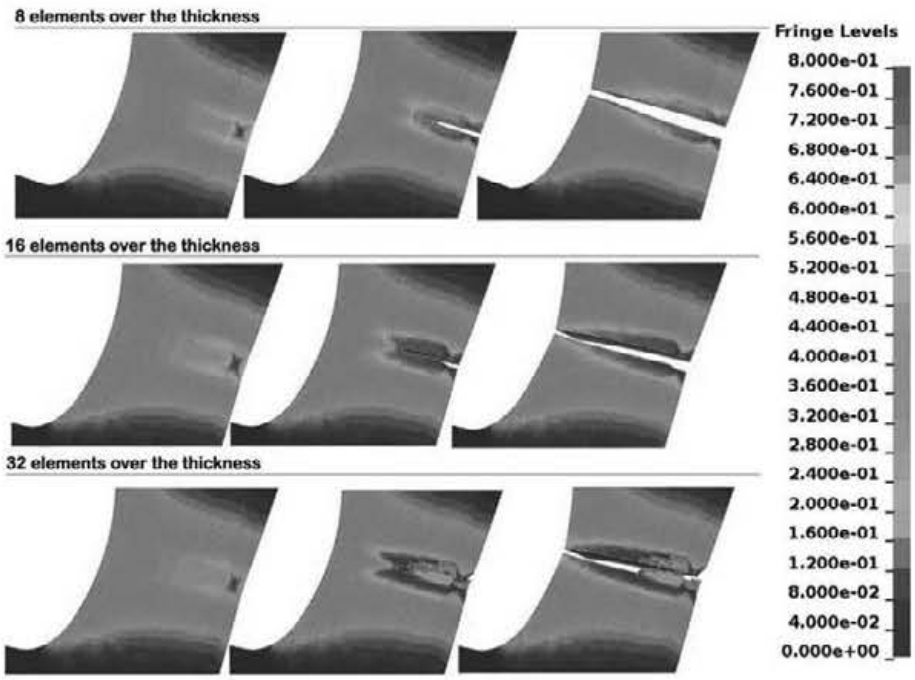

Fig. 19. From left to right, numerical simulations of the fracture sequence on the plane strain specimens. The last image from each row shows the fracture pattern created depending on the mesh size. Damage contours are plotted in the images.

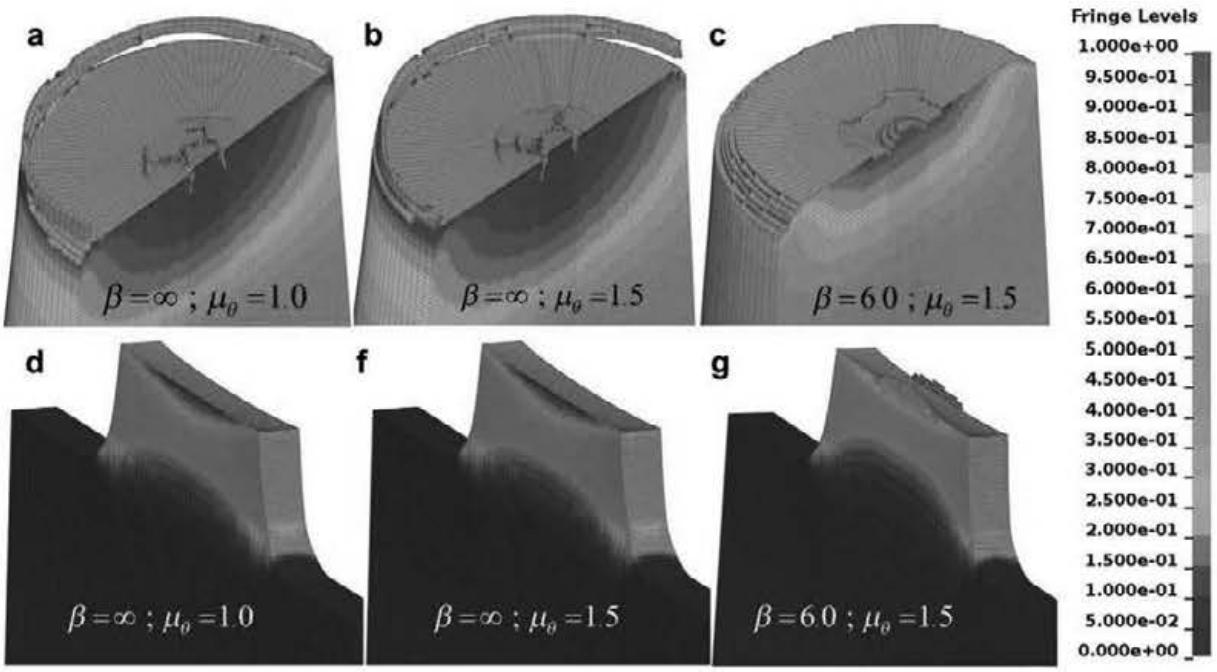

Fig. 20. Fracture surfaces obtained from the numerical simulations of three different cases: regular Johnson–Cook (a,d), JCXd without weakening (b,e) and JCXd (c,f). (Top) Smooth axisymmetric specimen with 144 elements across the diameter. (Bottom) Plane strain specimen with 32 elements over the thickness.

are plotted in Fig. 20(a), (b) and (c), respectively. The figures show damage contour plots from $D = 0.0$ to $D = 1.0$. The upper part of the specimens was removed and the rest was cut in half order to check the damage evolution of the internal elements. Quite similar result was obtained for the cases without weakening, cases (i) and (ii). An almost flat fracture surface can be seen comparing Fig. 20(a) and (b). Fig. 20(c) shows the fracture surface for the case (iii) that presented, in contrast to the other two cases, a successful cup-cone fracture pattern.

The numerical simulations of the plane strain specimen gave the fracture surfaces that are depicted in Fig. 20(d), (f) and (g). Such figures show damage contour plots and correspond to the cases (i), (ii) and (iii), respectively. The upper parts were removed for the sake of clarity. The cases (i) and (ii) gave identical fracture patterns, i.e. flat surface. The simulation ran with the JCXd material model, case (iii), was the only successful case in predicting the slanted fracture of the plane strain specimen. It can be then concluded that both effects,

the weakening and the Lode angle dependency in the failure criterion, were needed for a successful fracture prediction.

7. Concluding remarks

A coupled elastoplastic-damage material model for ballistic applications was proposed. The model accounted for the third deviatoric invariant dependency. Such a dependency was included in the model with the Lode angle dependent function in the equivalent plastic strain to failure expression of the Johnson–Cook failure criterion. The model also accounts for the weakening of the elastic moduli and constitutive relation, introducing implicitly the Lode angle dependency in the elastoplastic model of the material.

The model, designated as Johnson–Cook–Xue-damage (JCXd), was implemented in LS-DYNA non-linear finite element code by means of a user-defined subroutine programmed in FORTRAN programming language.

The JCXd material model was calibrated for the precipitation hardening Inconel 718 nickel-base superalloy. In order to calibrate the model three groups of mechanical tests were performed:

- Quasi-static tensile tests of axisymmetric smooth and notched specimens.
- Dynamic tensile tests of axisymmetric smooth specimens at various temperatures.
- Quasi-static tensile tests of shear and plane strain specimens.

An iterative calibration procedure through using numerical simulation of all the tests was performed. The final numerical simulations run with the calibrated constants were in good agreement with the experimental data. However, the elastoplastic behaviour corresponding to the tensile test of shear specimens was not well predicted.

A numerical study in terms of fracture pattern reproducibility was made by using the calibrated JXCd material model for precipitation hardened Inconel 718 nickel-base superalloy. Fracture pattern of the shear specimen was easily reproduced. Conversely, to obtain the desired fracture patterns of plane strain and axisymmetric smooth specimens an additional mesh sensitivity study was carried out. In order to prove that the discretisation was not the responsible of such fracture patterns, the effect of the weakening and the Lode angle was analysed. The main conclusion that came out from such an analysis is that both, the weakening and the Lode angle dependency in the failure criterion, were needed to predict complex fracture patterns.

Acknowledgements

The financial support that the Secretaría de Estado de Investigación, Desarrollo e Innovación of the Ministerio de Economía y Competitividad has given through the Project BIA2011-24445 is greatly acknowledged, as is, the contribution of Industria de Turbopropulsores (ITP).

The authors would like to thank the financial support and contribution to this work from the Structural Impact Laboratory (SIMLab), Centre for Research-based Innovation (CRI) at the Norwegian University of Science and Technology (NTNU).

References

Arthington, M.R., Siviour, C.R., Petrinic, N., Elliott, B.C.F., 2009. Cross-section reconstruction during uniaxial loading. Measurement Science and Technology 20, 075701.

Arthington, M.R., Siviour, C.R., Petrinic, N., 2012. Improved materials characterisation through the application of geometry reconstruction to quasi-static and high-strain-rate tension tests. International Journal of Impact Engineering 46, 86–96.

Bai, Y., Wierzbicki, T., 2008. A new model of plasticity and fracture with pressure and Lode dependence. International Journal of Plasticity 24, 1071–1096.

Bai, Y., Wierzbicki, T., 2010. Application of extended Mohr–Coulomb criterion to ductile fracture. International Journal of Fracture 161, 1–20.

Bao, Y., Wierzbicki, T., 2004. On fracture locus in the equivalent strain and stress triaxiality space. International Journal of Mechanical Sciences, 81–98.

Barsoum, I., Faleskog, J., 2007. Rupture mechanism in combined tension and shear – experiments. International Journal of Solids and Structures 44, 1768–1786.

Besson, J., Steglich, D., Brocks, W., 2001. Modeling of crack growth in round bars and plane strain specimens. International Journal of Solids and Structures 38, 8259–8284.

Børvik, T., Hopperstad, O.S., Berstad, T., Langseth, M., 2001. A computational model of viscoplasticity and ductile damage for impact and penetration. European Journal of Mechanics – A/Solids 20, 685–712.

Børvik, T., Hopperstad, O.S., Berstad, T., 2003. On the influence of stress triaxiality and strain rate on the behaviour of a structural steel. Part II. Numerical study. European Journal of Mechanics – A/Solids 22, 15–32.

Børvik, T., Hopperstad, O.S., Dey, S., Pizzinato, E.V., Langseth, M., Albertini, C., 2005. Strength and ductility of Weldox 460 E steel at high strain rates, elevated temperatures and various stress triaxialities. Engineering Fracture Mechanics 72, 1071–1087.

Bridgman, P.W., 1952. Studies in Large Flow and Fracture. McGraw-Hill, New York.

Chocron, S., Erice, B., Anderson, C.E., 2011. A new plasticity and failure model for ballistic application. International Journal of Impact Engineering 38, 755–764.

Cockcroft, M.G., Latham, D.L., 1968. Ductility and workability of metals. Journal of the Institute of Metals, 33–39.

Dey, S., Børvik, T., Hopperstad, O.S., Langseth, M., 2006. On the influence of fracture criterion in projectile impact of steel plates. Computational Material Science 38, 176–191.

Erice, B., 2012. Flow and fracture behaviour of high performance alloys. Ph.D. Thesis, Universidad Politécnica de Madrid (UPM), Madrid, Spain. <http://oa.upm.es/14461/1/Borja_Erice_Echavarri.pdf>.

Erice, B., Gálvez, F., Cendón, D.A., Sánchez-Gálvez, V., 2012. Flow and fracture behaviour of FV535 steel at different triaxialities, strain rates and temperatures. Engineering Fracture Mechanics 79, 1–17.

Eriksson, M., Lademo, O.G., Hopperstad, O.S., 2006. Development and use of in-plane shear tests to identify ductile failure parameters of aluminium alloys. In: 9th International Conference on Material Forming (ESAFORM-2006), Glasgow, pp. 331–334.

Fagerholt, E., Dorum, C., Borvik, T., Laukli, H.I., Hopperstad, O.S., 2010. Experimental and numerical investigation of fracture in a cast aluminium alloy. International Journal of Solids and Structures 47, 3352–3365.

Fourmeau, M., Borvik, T., Benallal, A., Lademo, O.G., Hopperstad, O.S., 2011. On the plastic anisotropy of an aluminium alloy and its influence on constrained multiaxial flow. International Journal of Plasticity 27, 2005–2025.

Gruben, G., Fagerholt, E., Hopperstad, O.S., Børvik, T., 2011. Fracture characteristics of a cold-rolled dual-phase steel. European Journal of Mechanics – A/Solids 30, 204–218.

Gruben, G., Hopperstad, O.S., Børvik, T., 2012. Evaluation of uncoupled ductile fracture criteria for the dual-phase steel Docol 600DL. International Journal of Mechanical Sciences 62, 133–146.

Hill, R., 1950. The Mathematical Theory of Plasticity. Oxford University Press, Oxford.

Johnson, G.R., Cook, W.H., 1983. A constitutive model and data for metals subjected to large strains, high strain rates and high temperatures. In: 7th International Symposium on Ballistics, The Hague, pp. 541–547.

Johnson, G.R., Cook, W.H., 1985. Fracture characteristics of three metals subjected to various strains, strain rates, temperatures and pressures. Engineering Fracture Mechanics 21, 31–48.

Kane, A., Børvik, T., Berstad, T., Benallal, A., Hopperstad, O.S., 2011. Failure criteria with unilateral conditions for simulation of plate perforation. European Journal of Mechanics – A/Solids 30, 468–476.

Kolsky, H., 1963. Stress Waves in Solids. Dover Publications, New York.

Le Roy, G., Embury, J.D., Edwards, G., Ashby, M.F., 1981. A model of ductile fracture based on the nucleation and growth of voids. Acta Metallurgica 29, 1509–1522.

Lemaitre, J., 1996. A Course on Damage Mechanics, second ed. Springer-Verlag, Berlin.

LS-DYNA KEYWORD USER'S MANUAL Version 971, 2007. Livermore Software Technology Corporation, Livermore, California.

Lubliner, J., 1990. Plasticity Theory. Macmillan, New York.

Mae, H., Teng, X., Bai, Y., Wierzbicki, T., 2007. Calibration of ductile fracture properties of a cast aluminium alloy. Materials Science and Engineering A 459, 156–166.

Mirone, G., Corallo, D., 2010. A local viewpoint for evaluating the influence of stress triaxiality and Lode angle on ductile failure and hardening. International Journal of Plasticity 26, 348–371.

Nahshon, K., Hutchinson, J.W., 2008. Modification of the Gurson model for shear failure. European Journal of Mechanics – A/Solids, 1–17.

Rice, J.R., Tracey, D.M., 1969. On the ductile enlargement of voids in triaxial stress fields. Journal of the Mechanics and Physics of Solids 17, 201–217.

Souza, E.A., Peric, D., Owen, D.R.J., 2008. Computational Methods for Plasticity. Theory and Applications. John Wiley & Sons Ltd., Chichester, West Sussex, United Kingdom.

Walker, J.D., Impact and Penetration Mechanics, 2013, in preparation.
Wilkins, M.L., Streit, R.D., Reaugh, J. E., 1980. Cumulative-strain-damage model of ductile fracture: simulation and prediction of engineering fracture tests. Lawrence Livermore National Laboratory, Livermore, California.
Xue, L., 2007. Damage accumulation and fracture initiation in uncracked ductile solids subject to triaxial loading. International Journal of Solids and Structures 44, 5163–5181.
Xue, L., 2009. Stress based fracture envelope for damage plastic solids. Engineering Fracture Mechanics, 419–438.
Xue, L., Wierzbicki, T., 2008. Ductile fracture initiation and propagation modeling using damage plasticity theory. Engineering Fracture Mechanics 75, 3276–3293.
Xue, L., Wierzbicki, T., 2009. Numerical simulation of fracture mode transition in ductile plates. International Journal of Solids and Structures, 1423–1435.